IOP Publishing and International Atomic Energy Agency Nuclear Fusion
Nucl. Fusion **48** (2008) 092002 (6pp) doi:10.1088/0029-5515/48/9/092002

LETTER

Tearing mode structure in the DIII-D tokamak through spectrally filtered fast visible bremsstrahlung imaging

M.A. Van Zeeland[1], J.H. Yu[2], M.S. Chu[1], K.H. Burrell[1], R.J. La Haye[1], T.C. Luce[1], R. Nazikian[3], W.M. Solomon[3] and W.P. West[1]

[1] General Atomics, PO Box 85608 San Diego, CA 92186-5608, USA
[2] University of California-San Diego, La Jolla, California, USA
[3] Princeton Plasma Physics Laboratory, Princeton, New Jersey, USA

E-mail: vanzeeland@fusion.gat.com

Received 21 March 2008, accepted for publication 9 July 2008
Published 5 August 2008
Online at stacks.iop.org/NF/48/092002

Abstract
Time evolved measurements of the detailed 2D poloidal structure of rotating tearing modes in the DIII-D tokamak are obtained for the first time using spectrally filtered fast imaging of broadband visible bremsstrahlung emission (N_B). Measurements are made along 256 × 256 different sightlines and show excellent agreement with simulations assuming a rotating helical $m/n = 2/1$ island structure superimposed on the equilibrium N_B profile. The method described here is capable of imaging with high resolution the structure of coherent oscillations in the core of current and next-step fusion plasma experiments such as ITER and can be applied to virtually any mode with a finite perturbed N_B and frequency in the laboratory frame provided sufficient signal level and detector bandwidth are available.

PACS numbers: 52.35.Py, 52.55.Fa, 52.70.Kz, 52.55.Tn

(Some figures in this article are in colour only in the electronic version)

M This article features online multimedia enhancements

1. Introduction

Tearing modes (TMs) and other MHD instabilities such as sawteeth can limit plasma pressure, significantly reduce confinement and induce harmful disruptions [1, 2]. TMs are also of interest because they can have beneficial effects, such as in the hybrid scenario where a $m/n = 3/2$ (m/n = poloidal/toroidal mode number) neoclassical tearing mode (NTM) elevates the central safety factor (q) above 1, avoiding the onset of sawteeth [2, 3]. In order to have confidence in our ability to monitor, control and predict these types of instabilities and their nonlinear consequences in future devices such as ITER, a detailed understanding of their internal structure and temporal evolution is essential. Virtually all measurements of the spatial structure of TMs and other instabilities in the core of existing tokamaks, however, are limited to small regions of the plasma or radial arrays; extracting 2D information often requires assumptions about the underlying structure to carry out tomographic inversion with a limited number of sightlines. As a result, the inferred mode profiles often lack the resolution required for detailed validation of state-of-the-art modelling. The advantage of 2D imaging can be seen from recent measurements of electron cyclotron emission on a poloidal cross-section, which have been used to identify significant shortcomings of leading sawtooth oscillation models as well as to investigate the effects of heating on NTMs through observation of mode-induced electron temperature fluctuations [4, 5].

In this letter, we demonstrate for the first time the use of a fast framing camera (26 kFrames s^{-1}) to image with unprecedented resolution (0.05–0.2 cm^2 along 6.5 × 10^4 sightlines) the 2D poloidal structure of a $m/n = 2/1$ TM in the core of a plasma rotating at ≈10 kHz in the DIII-D tokamak, and the subsequent modelling of these measurements. The

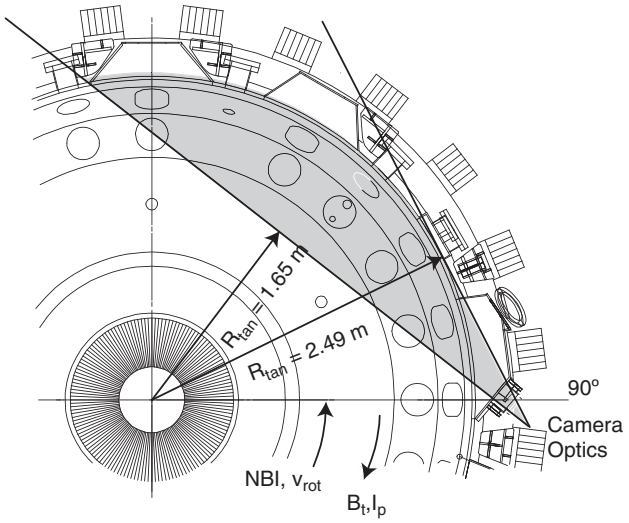

Figure 1. Plan view of the DIII-D tokamak showing the camera viewing region—grey. Minimum and maximum tangency radii are shown, $R_{\rm tan} = 1.65$ m and 2.49 m, respectively. Arrows indicate the direction of toroidal rotation ($v_{\rm rot}$), NBI, toroidal field ($B_{\rm t}$) and plasma current ($I_{\rm p}$).

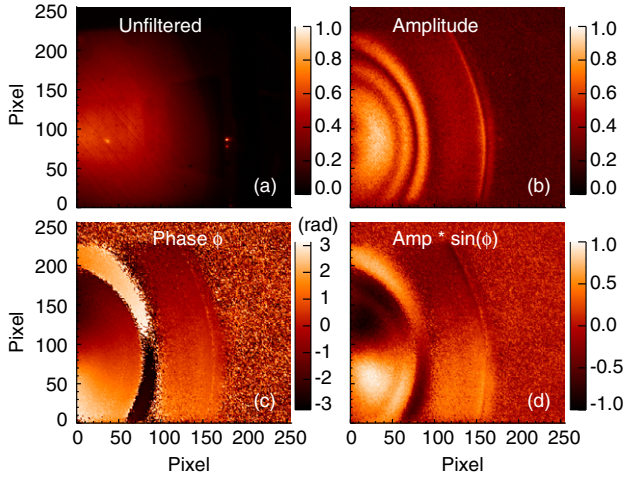

Figure 2. Discharge #131364, $t = 2165$ ms, fast camera data: (*a*) visible light emission with no frequency filtering, (*b*) Fourier amplitude ($\tilde{I}$) of each pixel's 512 point time series filtered at mode frequency 10.4 kHz, (*c*) phase (ϕ) of each pixel at mode frequency, (*d*) amplitude times sin(ϕ) from (*b*) and (*c*).

measurement region covered in a single frame is extremely large, with a projected cross sectional area that is 40% of the plasma itself (0.75 m^2/1.8 m^2).

2. Technique and experimental results

The light being imaged is broadband visible bremsstrahlung emission ($N_{\rm B}$) given by

$$\frac{{\rm d}N_{\rm B}}{{\rm d}\lambda} = 2.27 \times 10^{-14} \frac{n_{\rm e}^2 Z_{\rm eff}}{\lambda T_{\rm e}^{1/2}} {\rm e}^{-hc/\lambda T_{\rm e}}, \qquad (1)$$

where λ is the wavelength in Angstroms, $n_{\rm e}$ is the electron density in (cm^{-3}), $T_{\rm e}$ is the electron temperature in (eV) and ${\rm d}N_{\rm B}/{\rm d}\lambda$ is in photons cm^{-3} Å^{-1} s^{-1} sr^{-1}. The fluctuation in bremsstrahlung emission ($\tilde{N}_{\rm B}$) induced by a TM is given approximately by $\tilde{N}_{\rm B} \propto \xi \cdot \nabla N_{\rm B}$ where ξ is the radial field line displacement of the helical mode. Due to the $n_{\rm e}^2$ dependence, $\tilde{N}_{\rm B}$ is primarily a measure of mode-induced density fluctuations. Historically, visible $N_{\rm B}$ measurements have been used on a single channel basis for the study of MHD modes as well as incoherent fluctuations [6], while 1D and 2D high-resolution imaging of the visible continuum radiation has been done on a slow timescale to infer background plasma $Z_{\rm eff}$ profiles [7, 8]. In terms of fluctuation profile measurements, the most detailed results have been made using multi-channel linear arrays and more recently tangential imaging viewing the x-ray portion of the bremsstrahlung emission spectrum [9, 10]. Here, we describe wide-angle $\tilde{N}_{\rm B}$ measurements of a 2/1 TM exhibiting both high-spatial and temporal resolution. It should be pointed out that high-resolution measurements using similar technology to that presented here have been made outside of the core plasma, in the scrape-off-layer region, by studying D_α emission. Examples include the study of edge localized mode (ELM) dynamics [11] and edge turbulence using an injected D_2 gas puff [12].

Figure 1 shows a plan view of the DIII-D tokamak midplane as well as the focal plane of the fast framing camera and viewable region (shaded grey). The semi-tangential view spans from inside the magnetic axis to well outside the separatrix at $R \approx 2.25$ m. The spatial resolution of the detector is 256 × 256 pixels with 1 pixel imaging 0.05–0.2 cm^2 at the point of tangency, where the exact size depends on the location within the field of view. At this resolution, the camera is capable of storing 21 685 frames in one continuous time series with a maximum frame rate of 26 000 frames s^{-1}; as a result, it is possible to resolve, through spectral analysis, coherent oscillations with frequencies below the Nyquist limit of 13 kHz. Also shown in figure 1 is the direction of toroidal field ($B_{\rm t}$), plasma current ($I_{\rm p}$), toroidal rotation ($v_{\rm rot}$) and neutral beam injection (NBI) for the discharge discussed here.

Figure 2(*a*) shows a typical frame in false colour of the total light emission in the range $\lambda \approx$ 450–900 nm taken during an attempted quiescent H-mode plasma with $n_{\rm e} = 7 \times 10^{13}$ cm^{-3}, $T_{\rm e}(0) = 1.4$ keV, $T_{\rm i}(0) = 1.5$ keV, $B_{\rm T} = 2$ T and $\bar{Z}_{\rm eff} = 3$–4. A time sequence of these raw images shows no obvious fluctuations or motion despite the presence of a $m/n = 2/1$ TM rotating at 10 kHz (n (m) is identified from a toroidal (poloidal) array of unequally spaced Mirnov coils with an amplitude at the wall of $\delta B_\theta / B_{\rm t} \approx 4 \times 10^{-4}$). At the timestep shown in figure 2, the normalized beta ($\beta_{\rm N}$) is 0.86, which has decreased from its peak of $\beta_{\rm N} = 1.5$ due to the 2/1 mode. Although the exact nature of the mode itself is not critical to the work presented here, it is referred to as a TM, because the mode appears to grow initially due to classical processes. At the time shown in figure 2, the cylindrical equivalent of the tearing mode stability index (Δ') computed by the linear PEST-III code [13] is 1.222 m^{-1}, and the dimensionless equivalent stability index ($r_{\rm s}\Delta'$) is approximately 0.39. There is experimental indication, however, that bootstrap current is playing a role in determining the island saturation at the time of interest so the designation NTM may also be appropriate.

Through spectral analysis of each pixel's time series, the structure of the 2/1 mode is visualized. Figure 2(*b*) shows the normalized Fourier amplitude ($\tilde{I}$) of each pixel at the mode frequency identified by magnetics, where the peak $\tilde{I}/I \approx 1\%$.

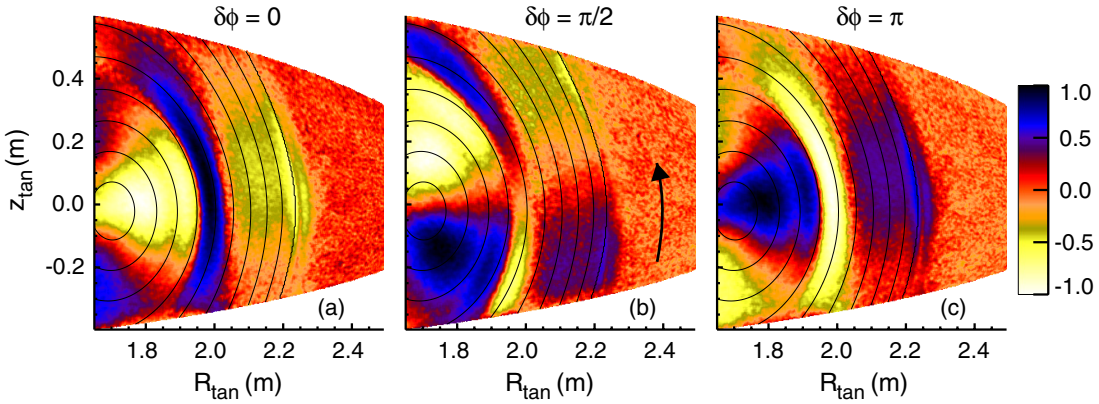

Figure 3. Amplitude and phase data from figure 2 as $\tilde{I}\cos(\phi + \delta\phi)$ mapped to $(R_{\rm tan}, z_{\rm tan})$ coordinates showing the counter-clockwise mode rotation direction (arrow in (*b*)). The overlayed black curves are equally spaced contours of $\rho = 0.1$–1.0 at tangency locations. (*a*) $\delta\phi = 0$, (*b*) $\delta\phi = \pi/2$, (*c*) $\delta\phi = \pi$.

This figure is dramatically different from the unfiltered image shown in figure 2(*a*) and is a direct measurement of the 2D spatial profile of the visible bremsstrahlung emissivity perturbed by the 2/1 mode as viewed along 6.5×10^4 different sightlines. In figure 2(*c*) the corresponding phase (ϕ) of each pixel in the analysed time interval at the mode rotation frequency is shown. The 2D phase structure clearly exhibits a large region over which the phase of adjacent pixels are correlated. Outside of horizontal pixel ≈175, the camera view is outside of the separatrix (black region in figure 2(*a*)) and, as one would expect, the phase of adjacent pixels in this region are completely uncorrelated. In figure 2(*d*), $\tilde{I}\sin(\phi)$ is plotted and the $m = 2$ nature of the observed perturbation becomes clear. Figure 2(*d*) is equivalent to a snapshot in time of the 2/1 mode.

Using the viewing trajectory from the camera, the image data are mapped to toroidal magnetic flux coordinates. For each pixel, the major radius (R) and vertical height (z) are obtained at the point $R_{\rm tan}$ where the line of sight is tangent to a flux surface. The flux-tangency point is chosen for this mapping because each pixel's line of sight intersects the largest volume of flux-confined emission in this region. The fluctuating 10 kHz $N_{\rm B}$ image shown in figure 2(*d*) is replotted in figure 3 but now mapped to $(R_{\rm tan}, z_{\rm tan})$ coordinates. A pseudo-time sequence is generated in this figure by plotting $\tilde{I}\cos(\phi + \delta\phi)$, where $\delta\phi$ is a phase increment (equivalent to toroidal angle at a given time or increasing time at a given toroidal location), and the successively increasing values serve to show the counter-clockwise direction of rotation of the 2/1 mode. This corresponds to plasma rotation in the counter-current direction, as confirmed by charge exchange recombination (CER) measurements. A movie of the rotating mode structure is available online for download at stacks.iop.org/NF/48/092002.

Overlaid in figures 3(*a*)–(*c*) are contours of the square root of normalized toroidal flux (equally spaced from $\rho = 0.1$–1.0) mapped to the point of tangency. The flux contours, obtained using the EFIT magnetic equilibrium reconstruction code, add perspective to the mode structure and clearly show the centering at the magnetic axis as well as a sharp drop in amplitude at the separatrix. Similar to the discussion of figure 2(*c*), outside the separatrix, the amplitude is essentially zero and an analysis of the coherence between each pixel with a pixel near the magnetic axis showed levels well below the 95% confidence level.

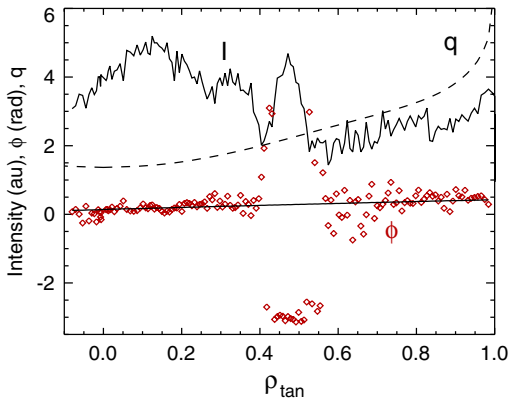

Figure 4. Data from figure 3(*a*) taken along the horizontal line through $z = 0$, showing: (solid) spectral amplitude $\tilde{I}$ at mode frequency, (diamonds) phase, (dashed) q-profile. The solid overlayed line through the phase is the prediction for radial phase offset due to viewing the geometry for an $n = 1$ mode.

The poloidal structures shown in figures 3(*a*)–(*c*) exhibit a phase inversion at the $q = 2$ surface location ($\rho \approx 0.4$), where theory predicts the TM island to be centred. The phase inversion and its exact q location are further illustrated in figure 4 by plotting the amplitude and phase variation along a radial segment for a horizontal line centred at $z = 0$. The π phase inversion as measured by the fast camera occurs near $\rho \approx 0.42$ as compared with $\rho \approx 0.40$ where the overlayed q-profile shows $q = 2$. This level of agreement is well within the combined errors of the EFIT reconstruction ($\rho = 0.40 \pm 0.05$) and line-of-sight mapping. Another confirmation of the $q = 2$ surface location is obtained from CER measurements of the toroidal rotation velocity which places the 10 kHz rotation frequency at $\rho = 0.45$.

Also shown in figure 4 is an overall increasing trend in the phase 'baseline' as one moves from the core to the edge. This can be understood when one considers that each viewing ray has its $R_{\rm tan}$ at a different toroidal location $\phi_{\rm tor}$ and the mode has a toroidal mode number of $n = 1$; thus, one would expect a slight phase variation given by $n\phi_{\rm tor}(R_{\rm tan})$. The solid overlayed line represents the calculated phase variation due to this effect

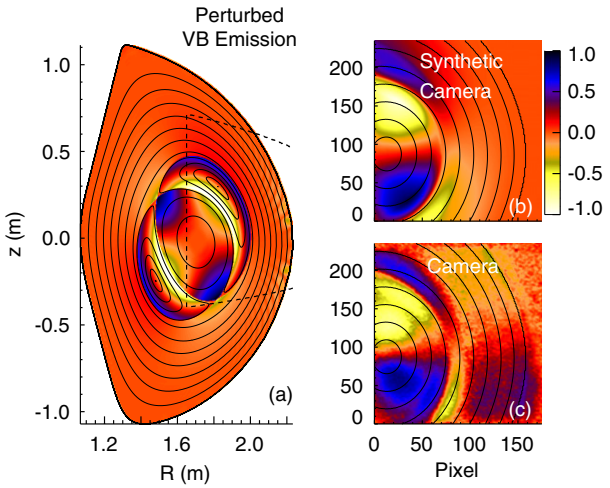

Figure 5. TM modelling. (*a*) Calculated $\tilde{N}_B$ at one toroidal phase for 2/1 TM. The overlayed solid contours indicate isosurfaces of helical flux showing the island structure. The overlayed dashed line indicates the region imaged at tangency locations. (*b*) Synthetic camera diagnostic prediction for measured intensity perturbation at a single timestep due to 2/1 mode. (*c*) Actual camera image to be compared with synthetic diagnostic in (*b*).

for an $n = 1$ mode which matches the data extremely well. Interestingly, this points to the possibility of exploiting this geometrical effect as a diagnostic for toroidal mode number that will be increasingly useful for higher n.

3. Modelling of measurements

One of the most beneficial aspects of such detailed mode measurements, and this new measurement capability in general, is the prospect for validating computational modelling at a level previously thought unobtainable. To demonstrate this process, a model for the helical equilibrium perturbation due to a 2/1 TM, as presented in [14], is adopted. The model assumes a perturbed poloidal flux ($\tilde{\Psi}$) given by

$$\tilde{\Psi}(\rho, \theta, \phi_{\rm tor}) = A_{m,n}(\rho)\cos(m\theta - n\phi_{\rm tor} - \phi_{nm}), \quad (2)$$

where θ is the poloidal angle coordinate and ϕ_{nm} determines the island phase. The amplitude function $A_{m,n}$ is defined by

$$A_{m,n} = c_0\rho^{k_1/2}(1-\rho)^{k_2}, \quad (3)$$

where the parameters $c_0 = 0.31$, $k_1 = 6.5$, $k_2 = 5.0$ are chosen to match the induced full island width to estimates ($W \approx 12$ cm on outboard midplane) based on experimental data. In this study, island width estimates were made using equation (13) from [15] which uses amplitude information from edge magnetic signals in combination with the magnetic equilibrium calculated by EFIT. The $\theta(R, z)$ values were calculated using the PEST-III code [13] which also takes the EFIT calculated magnetic equilibrium as an input. The variation in the 'radial' width of the island comes from the 'radial' density of flux surfaces from EFIT, as the island should be of constant width in the poloidal flux coordinate.

Figure 5(*a*) shows the calculated profile at one time/toroidal location of the TM induced perturbed visible bremsstrahlung emission (surface) overlayed with contours of helical flux (solid curves). The three-dimensional helical flux function $F = F_0 + F_1$ has an equilibrium part $F_0 = n\Phi_0 - m\Psi_0$ and a perturbed part $F_1 = -m\tilde{\Psi}$, where Φ_0 and Ψ_0 are the unperturbed toroidal and poloidal fluxes, respectively. $\tilde{N}_B(R, z)$ was calculated by mapping the experimentally measured $N_B(F_0)$ to the perturbed $N'_B(F)$ locations and taking the difference. Inside of the island structures, N'_B is assumed to be uniform and was set equal to the equilibrium N_B at the $q = 2$ surface. The equilibrium bremsstrahlung emissivity profile $N_B(F_0)$ is obtained from a calibrated radial array of photodiodes. In figure 5(*a*), both the helical flux contours and the $\tilde{N}_B$ clearly show the 2/1 magnetic island structure. To help convey the large portion of the plasma that is imaged, the bounds of the region viewed by the camera at the tangency radii are overlayed as dashed lines.

To simulate the camera measurements, a synthetic diagnostic was created which integrates the perturbed bremsstrahlung emissivity along the viewing trajectory of each pixel and properly includes the $n = 1$ toroidal mode variation. A synthetic camera frame is arrived at by averaging each pixel view over the same phase variation of the rotating mode covered in one exposure time, and a time series 'movie' is generated by creating a sequence of such images. This allows exactly the same spectral analysis techniques to be applied to the simulated dataset as were applied to the original camera frames and permits a one-to-one comparison.

Plotted in figure 5(*b*) is the simulated camera image of mode-induced fluctuating pixel intensity to be compared with the actual image shown in figure 5(*c*). For reference the contours of ρ at the point of tangency have been overlayed. The simulation and data shown in figures 5(*b*) and (*c*) certainly exhibit qualitative agreement with many strikingly similar characteristics as well as some differences. One point of agreement is that the phase inversion at the island radial location ($\rho \approx 0.4$) does not exactly follow the flux surface. The width of the perturbation also appears to become extended at higher z. This is purely a consequence of the line-integrated nature of the view. Also, the simulation predicts an apparent perturbed emission at radii well inside of the $q = 2$ surface, as also observed in figure 5(*c*), some of which is due to line integration. One point of disagreement that cannot be reconciled given the mode structure plotted in figure 5(*a*) is the presence of a separate phase inversion at $\rho \approx 0.6$ and another significant low-m perturbation outside of this radius. This may be due to another separate mode, or sideband, not included in the simulations and will be further addressed by a full multimode nonlinear simulation with the NIMROD code.

The identification of the phase and structure of TMs is particularly important since accurate ECCD alignment and modulation is required for NTM control. One artifact resulting from the tangential view, that can be easily removed, is the apparent phase variation due to different tangency locations for the different channels. For a given toroidal mode number n, a simple phase subtraction $n\phi_{\rm tor}(R_{\rm tan})$ essentially brings each pixel to the same toroidal angle at the point of tangency. Of course the toroidal mode number needs to be known. Extrapolation to any other toroidal angle is then simple. Estimation of the island width and location is complicated by the fact that for any view passing through an island, all points

along the ray will contribute to the measurement. The net effect is to shift the apparent centre of the island projection to smaller major radii. In general, line-integrated effects complicate the interpretation of camera images and in practice a combination of real time inversion or forward modelling will be needed to compensate for the effect of the toroidal projection. A thorough analysis of these issues will be the subject of future work.

4. Projections to ITER and future devices

ITER and other future devices will be equipped with both visible and infrared imaging systems to monitor divertor and wall temperature as well as other more transient events. The tangential ITER wide-angle viewing system, planned for equatorial port 1, will have an optical view of the entire plasma cross section [16]. This view can in principle be used for MHD imaging. To address the applicability of this new imaging technique to ITER, the total N_B integrated over the wavelength region 450–900 nm is evaluated for typical ITER parameters estimated to be approximately $n_e = 10 \times 10^{13}\,\mathrm{cm}^{-3}$, $T_e(0) = 15\,\mathrm{keV}$, $\bar{Z}_{\mathrm{eff}} \approx 1.7$ [17], giving $N_B = 2.2 \times 10^{13}\,\mathrm{photons\,cm^{-3}\,s^{-1}\,sr^{-1}}$. This is to be compared with $N_B = 7 \times 10^{12}\,\mathrm{photons\,cm^{-3}\,s^{-1}\,sr^{-1}}$ for the plasma parameters of the DIII-D discharge discussed here. Using the same emissivity profile shape $[N_B(\rho)]$ as that from the previous section scaled to the peak central emissivity of $N_B = 2.2 \times 10^{13}\,\mathrm{photons\,cm^{-3}\,s^{-1}\,sr^{-1}}$ on ITER, simulations of the expected signal levels for the ITER midplane wide-angle viewing system have been carried out. While the local emissivities in ITER are less than those measured here, when integrated along the viewing sightlines they are very similar, owing to the longer pathlengths in ITER. For a midplane sightline with its tangency point at the magnetic axis, the resultant line-integrated bremsstrahlung emission, or equivalently surface radiance, $(N_B L)$ is approximately $N_B L = 1.8 \times 10^{16}\,\mathrm{photons\,cm^{-2}\,s^{-1}\,sr^{-1}}$ while that shown here is $N_B L = 1.6 \times 10^{16}\,\mathrm{photons\,cm^{-2}\,s^{-1}\,sr^{-1}}$.

In order to predict the actual photon flux arriving at a simulated ITER camera pixel and make comparisons with our DIII-D measurements, one must consider the optical systems involved. The ideal light throughput for a single pixel can be calculated using the area of the entrance pupil (A) and solid angle viewed by each pixel (Ω) combined to form the etendue (η), where $\eta = A\Omega$. The surface radiance of the viewing object multiplied by η is the maximum possible collected signal in photons s^{-1}. For the measurements described here, $\eta_{\mathrm{D3D}} \approx 3.0 \times 10^{-6}\,\mathrm{cm^2\,sr}$. While the exact optical system in ITER is not yet fully known, it is expected that the diameter of the imaging aperture (D) through the first wall will determine the maximum collection area which is estimated to be in the range $5\,\mathrm{mm} < D < 2\,\mathrm{cm}$ [18]. The total horizontal angle along the midplane required to span the entire ITER plasma cross-section is approximately 50°, and when imaged onto a row of 256 camera pixels, the solid angle viewed by each pixel is $\Omega = 1.16 \times 10^{-5}\,\mathrm{sr}$, giving $\eta_{\mathrm{ITER}} \approx 2.3$–$36 \times 10^{-6}\,\mathrm{cm^2\,sr}$ per pixel. Combining these calculations, the total photons s^{-1} (P_{ITER}) expected to arrive at a midplane central viewing ITER camera pixel scaled to the photon detection rate (P_{D3D}) from an equivalent DIII-D sightline are in the range $P_{\mathrm{ITER}}/P_{\mathrm{D3D}} = 0.8$–13. These results mean that for similar noise levels, frame rate and transmission attenuation one should expect the same camera used in these studies to clearly resolve modes of similar amplitude in ITER, where amplitude is defined as $\tilde{I}/I = \tilde{P}/P$ and is ≈1%. In fact, it is expected that the plasma rotation frequencies in ITER will be significantly lower allowing for longer integration times and even larger collected numbers of photons. Further, it is pointed out that fast framing camera systems with a more dynamic range (14 bits) are available as well as image intensifiers which will both help to increase the utility of this diagnostic.

5. Summary and conclusions

In summary, a technique for imaging coherent fluctuations in the core of fusion plasmas through fast framing camera images of visible bremsstrahlung emission (N_B) has been demonstrated in the DIII-D tokamak and has been used to obtain the detailed poloidal structure of a 2/1 TM rotating at 10 kHz. Taking advantage of the camera's fast sampling rate, a straightforward Fourier analysis of every pixel's time series allows us to obtain reconstructed images of mode phase and amplitude at over 10^4 different poloidal locations. Initial modelling of the measurement has been carried out assuming a rotating helical $m/n = 2/1$ island structure superimposed on the equilibrium N_B profile combined with a synthetic camera diagnostic that uses the camera viewing geometry, experimentally measured N_B profiles and estimates for the island width as inputs. The modelling-experiment comparison exhibits striking similarities in which many of the measured features are reproduced and explained. The extension of this technique to other MHD events and coherent fluctuations is straightforward and offers an opportunity for some of the most elaborate model validation to date. Additionally, higher-level spectral analysis tools such as singular value decomposition (SVD) [10] and correlation analysis with other diagnostics may further extend its usefulness and are being investigated.

The application of spectrally filtered visible bremsstrahlung imaging in future devices has been estimated using ITER as an example and the results show adequate signal levels owing to the higher densities and much longer path lengths. These results offer an exciting opportunity to obtain detailed core fluctuation measurements in next-step fusion plasmas.

This work was supported by the US Department of Energy under DE-FC02-04ER54698, DE-FG02-04ER54758, DE-AC02-76CH03073 and DE-FG02-07ER54917. The authors would like to thank Dr Dan Thomas and Dr Charlie Lasnier for providing design information and useful discussions relevant to the ITER projections in section 4.

References

[1] Hender T.C. *et al* 2007 *Nucl. Fusion* **47** S128
[2] La Haye R.J., Politzer P.A. and Brennan D.P. 2008 *Nucl. Fusion* **48** 015005
[3] Wade M.R. *et al* 2005 *Nucl. Fusion* **45** 407
[4] Park H.K. *et al* 2006 *Phys. Rev. Lett.* **96** 195004
[5] Classen I.G.J. *et al* 2007 *Phys. Rev. Lett.* **98** 035001
[6] Grek B., Bartolick J. and Johnson D. 1992 *Rev. Sci. Instrum.* **63** 4627

[7] Marmar E.S. *et al* 2001 *Rev. Sci. Instrum.* **72** 940
[8] Patel A., Carolan P.G., Conway N.J. and Akers R.J. 2004 *Rev. Sci. Instrum.* **75** 4944
[9] JET Team (prepared by Huysmans G.T.A.) 1999 *Nucl. Fusion* **39** 1965
[10] Ohdachi S. *et al* 2003 *Rev. Sci. Instrum.* **74** 2136
[11] Yu J.H., Boedo J.A., Hollmann E.M., Moyer R.A., Rudakov D.L. and Snyder P.B. 2008 *Phys. Plasmas* **15** 032504
[12] Zweben S.J. *et al* 2002 *Phys. Plasmas* **9** 1981
[13] Pletzer A. and Dewar R.L. 1991 *J. Plasma Phys.* **45** 427
[14] Strumberger E., Gunter S., Schwarz E. and Tichmann C. 2008 *New J. Phys.* **10** 023017
[15] La Haye R.J. *et al* 2000 *Phys. Plasmas* **7** 3349
[16] Thomas D.M., ITER Organization 2008 private communication
[17] Donne A.J.H. *et al* 2007 *Nucl. Fusion* **47** S337
[18] 2007 *Lawrence Livermore National Laboratory Report* UCRL-TR-228629, March 2007